# Structural Instability of Driven Josephson Circuits Prevented by an Inductive Shunt

Lucas Verney,[1,2] Raphaël Lescanne,[1,2] Michel H. Devoret,[3] Zaki Leghtas,[1,2,4] and Mazyar Mirrahimi[1,5,*]

[1] *QUANTIC team, INRIA de Paris, 2 Rue Simone Iff, 75012 Paris, France*

[2] *Laboratoire Pierre Aigrain, Ecole Normale Supérieure, PSL Research University, CNRS, Université Pierre et Marie Curie, Sorbonne Universités, Université Paris Diderot, Sorbonne Paris-Cité, 24 rue Lhomond, 75231 Paris Cedex 05, France*

[3] *Department of Applied Physics, Yale University, 15 Prospect Street, New Haven, Connecticut 06511, USA*

[4] *Centre Automatique et Systèmes, Mines-ParisTech, PSL Research University, 60, bd Saint-Michel, 75006 Paris, France*

[5] *Yale Quantum Institute, Yale University, New Haven, Connecticut 06520, USA*

(Received 25 May 2018; revised manuscript received 11 December 2018; published 1 February 2019)

Superconducting circuits are a versatile platform to implement a multitude of Hamiltonians that perform quantum computation, simulation, and sensing tasks. A key ingredient for realizing a desired Hamiltonian is the irradiation of the circuit by a strong drive. These strong drives provide an *in situ* control of couplings, which cannot be obtained by near-equilibrium Hamiltonians. However, as shown in this paper, out-of-equilibrium systems are easily plagued by complex dynamics, leading to instabilities. The prediction and prevention of these instabilities is crucial, both from a fundamental and application perspective. We propose an inductively shunted transmon as the elementary circuit optimized for strong parametric drives. Developing a numerical approach that avoids the built-in limitations of perturbative analysis, we demonstrate that adding the inductive shunt significantly extends the range of pump powers over which the circuit behaves in a stable manner.

DOI: 10.1103/PhysRevApplied.11.024003

## I. INTRODUCTION

Josephson junctions are ideal nondissipative elements that realize nonlinear Hamiltonians for superconducting quantum circuits. Compared to nonlinear crystals in the optical regime, Josephson circuits have a much larger ratio between multiwave mixing and decoherence rates [1–3]. By applying off-resonant drives (pumps) verifying frequency-matching conditions, one can engineer various Hamiltonians that are not obtainable statically. This so-called parametric method has been used, for instance, to achieve frequency conversion [4], quantum-limited amplification [5], two-mode squeezing [6], transverse readout of a qubit [7], and multiphoton exchanges between two modes [8]. In all these applications, the rates of the engineered parametric couplings scale with the pump power. However, as observed in Refs. [8–10], this scaling can be strongly limited by effects such as the induced deterioration of the coherence properties.

In this paper, we explain these limitations by analyzing the structural stability of the underlying dynamical system. We call a dynamical system structurally stable if small modifications of the parameters, such as the strength of the pumping drives, lead to small changes in its qualitative behavior, such as the asymptotic steady states of the driven-dissipative system. We show that the ubiquitous system consisting of a transmon [11,12] coupled to a cavity mode displays strong instabilities in this sense. We predict that above a critical pump power, the transmon state escapes the Josephson potential confinement and is sent to free-particle-like states. The circuit then behaves as if we had removed the junction and this explains the jump of the cavity frequency toward its bare (undressed) value, a phenomenon observed and used in the past for single-shot qubit readout [13]. Next, to prevent the instability caused by this escape from the confining potential, we propose to shunt the transmon with an inductance smaller than the kinetic inductance of the junction. We show that, as a result of the additional harmonic confinement, this system behaves in a stable manner over a wide range of pump strengths.

Nonperturbative numerical simulations of these strongly driven nonlinear systems are particularly challenging. They require the simulation of a master equation over a Hilbert space of large dimension and with time scales separated by many orders of magnitude [14]. Here, we

*mazyar.mirrahimi@inria.fr

 

treat the dimension problem by performing transformations that displace the high excitation manifold into a tractable one correctly (see Appendix A). Also, usually, to simplify the dynamics, one starts by removing the fast time scales through rotating-wave approximations. However, reliable simulations in the presence of strong drives require taking into account the counter-rotating terms in the Hamiltonian, the importance of which has been previously noted by [15,16]. Here, we avoid time-averaging the driven Hamiltonian, by using the Floquet-Markov theory [17] to characterize the asymptotic behavior of the system. The periodically driven Hamiltonian of a general circuit, subject to a single pump at frequency $\omega_p$ [Figs. 1(a) and 1(d)], can be expressed in the Floquet-states basis. These Floquet states $\{|\Psi_\alpha(t)\rangle\}_\alpha$, corresponding to $2\pi/\omega_p$-periodic orbits of the system, are the eigenstates of the time-dependent Hamiltonian associated with the eigenvalues $\{\epsilon_\alpha\}_\alpha$, which are called the Floquet quasienergies. For any Markovian bath, and in the weak coupling limit, one achieves an effective Floquet master equation for the evolution of the open quantum system. In the absence of resonances [[17], Section 9.3], this Floquet master equation admits, as the steady state, a limit cycle of period $2\pi/\omega_p$ given by $\rho_{ss}(t) = \sum_\alpha p_\alpha |\Psi_\alpha(t)\rangle \langle\Psi_\alpha(t)|$, a statistical mixture of Floquet states. The populations of these states are calculated through an extension of the Fermi golden rule to time-periodic systems [17] (also see Appendix B).

## II. THE DRIVEN TRANSMON AND STRUCTURAL INSTABILITY

We start by considering a transmon coupled to a harmonic oscillator (referred to in the following simply as an "oscillator"). The Hamiltonian of this circuit [shown in Fig. 1(a)] is given by

$$\mathbf{H}(t) = \hbar\omega_a \mathbf{a}^\dagger\mathbf{a} + 4E_C\mathbf{N}^2 - E_J\cos(\boldsymbol{\theta}) + i\hbar g\,\mathbf{N}\left(\mathbf{a}^\dagger - \mathbf{a}\right) + i\hbar\mathcal{A}_p(t)\left(\mathbf{a}^\dagger - \mathbf{a}\right). \quad (1)$$

Here, $\mathbf{N}$ and $\cos(\boldsymbol{\theta})$ are the transmon-mode operators corresponding to the number of Cooper pairs and their transfer across the junction, while $\mathbf{a}$ and $\mathbf{a}^\dagger$ are photon annihilation and creation operators of the oscillator. We note that here the phase $\boldsymbol{\theta}$ takes its values in the interval $[0, 2\pi]$ and only periodic operators such as $\cos(\boldsymbol{\theta}) = (\sum_N |N\rangle\langle N+1| + \text{H.c.})/2$ are well defined (here, the $|N\rangle$ are the charge states) [18]. Furthermore, $E_C$ is the charging energy, $E_J$ is the Josephson coupling energy, $\omega_a$ is the bare frequency of the oscillator in the absence of coupling to the transmon, and $g$ is the coupling rate between the two modes. The pump is described by $\mathcal{A}_p(t) = A_p\cos(\omega_p t)$, with an amplitude $A_p$ and a frequency $\omega_p$ far detuned from the resonance frequencies of the system. Throughout this paper, we consider, as the basis, the tensor products of the oscillator Fock states $\{|n\rangle\}_{n=0}^\infty$ and the transmon states $\{|\eta_k\rangle\}_{k=0}^\infty$ [eigenstates of the transmon Hamiltonian $4E_C\mathbf{N}^2 - E_J\cos(\boldsymbol{\theta})$]. We model the dissipation as a capacitive coupling of the oscillator to a transmission line [19]

$$\mathbf{H}_{SB} = \sum_k \hbar\omega_k \mathbf{c}^\dagger[\omega_k]\mathbf{c}[\omega_k] - \hbar\Omega[\omega_k](\mathbf{a}^\dagger - \mathbf{a})(\mathbf{c}^\dagger[\omega_k] - \mathbf{c}[\omega_k]). \quad (2)$$

Here, the modes $\mathbf{c}[\omega_k]$ are the bath modes and $\Omega[\omega_k]$ represents their coupling strengths to the mode $\mathbf{a}$.

We investigate the dynamics of this system for large pump amplitudes where the circulating photon number, given by $\bar{n} = |A_p|^2/4|\Delta_p|^2$ (with $\Delta_p$ the detuning between the pump frequency and the dressed oscillator frequency), can reach a few thousands. In order to reduce the required truncation of the Hilbert space, we consider a change of variables that takes into account such a coherent displacement of the oscillator. As shown in Appendix A, the new Hamiltonian is given by

$$\tilde{\mathbf{H}}(t) = \hbar\omega_a\tilde{\mathbf{a}}^\dagger\tilde{\mathbf{a}} + 4E_C\tilde{\mathbf{N}}^2 - E_J\cos\left[\tilde{\boldsymbol{\theta}} + \xi\sin(\omega_p t)\right] + i\hbar g\,\tilde{\mathbf{N}}\left(\tilde{\mathbf{a}}^\dagger - \tilde{\mathbf{a}}\right), \quad (3)$$

where $\xi = 2g\omega_a A_p/\left[\omega_p\left(\omega_a^2 - \omega_p^2\right)\right]$.

We perform Floquet-Markov-type simulations [20] assuming a white-noise spectrum for the bath. In Fig. 1(b), we plot the populations of the transmon eigenstates $\{|\eta_k\rangle\}_{k=0}^\infty$ in $\rho_{ss}(0)$ as a function of the pump power. We do not plot the populations in the mode $\tilde{\mathbf{a}}$, as the displaced oscillator remains close to its ground state. This confirms that the actual state is well approximated by a coherent state, as calculated in Appendix A. The dynamics of the displaced transmon mode exhibit two regimes. For $\bar{n} \lesssim 100$, the state remains pure [impurity given by the black crosses, right-hand axis, in Fig. 1(c)] close to the ground state, except for a few pump-power values. For $\bar{n} \gtrsim 100$, it rapidly turns into a mixed state of a high number of excitations, above the cosine confinement. Indeed, the number of confined states is roughly given by the ratio between the depth of the cosine potential ($2E_J$) and the level spacings (approximately $\sqrt{8E_JE_C}$) [11]. With the parameters used in Fig. 1, we obtain about eight confined levels.

Inspired by the experiments on the ac Stark shift [21,22], we simulate an excitation spectroscopy of such a driven system near the oscillator bare frequency. Each Floquet state $|\Psi_\alpha(t)\rangle$, with a nonzero population in the steady state $\rho_{ss}(t)$, can be excited to other Floquet states $|\Psi_\beta(t)\rangle$ by a weak probe drive at the frequency given by the difference of their quasienergies $(\epsilon_\beta - \epsilon_\alpha)/\hbar$ [16,23,24] (see also Appendix B). In Fig. 1(c), we plot all these resonance frequencies as a function of the pump power.

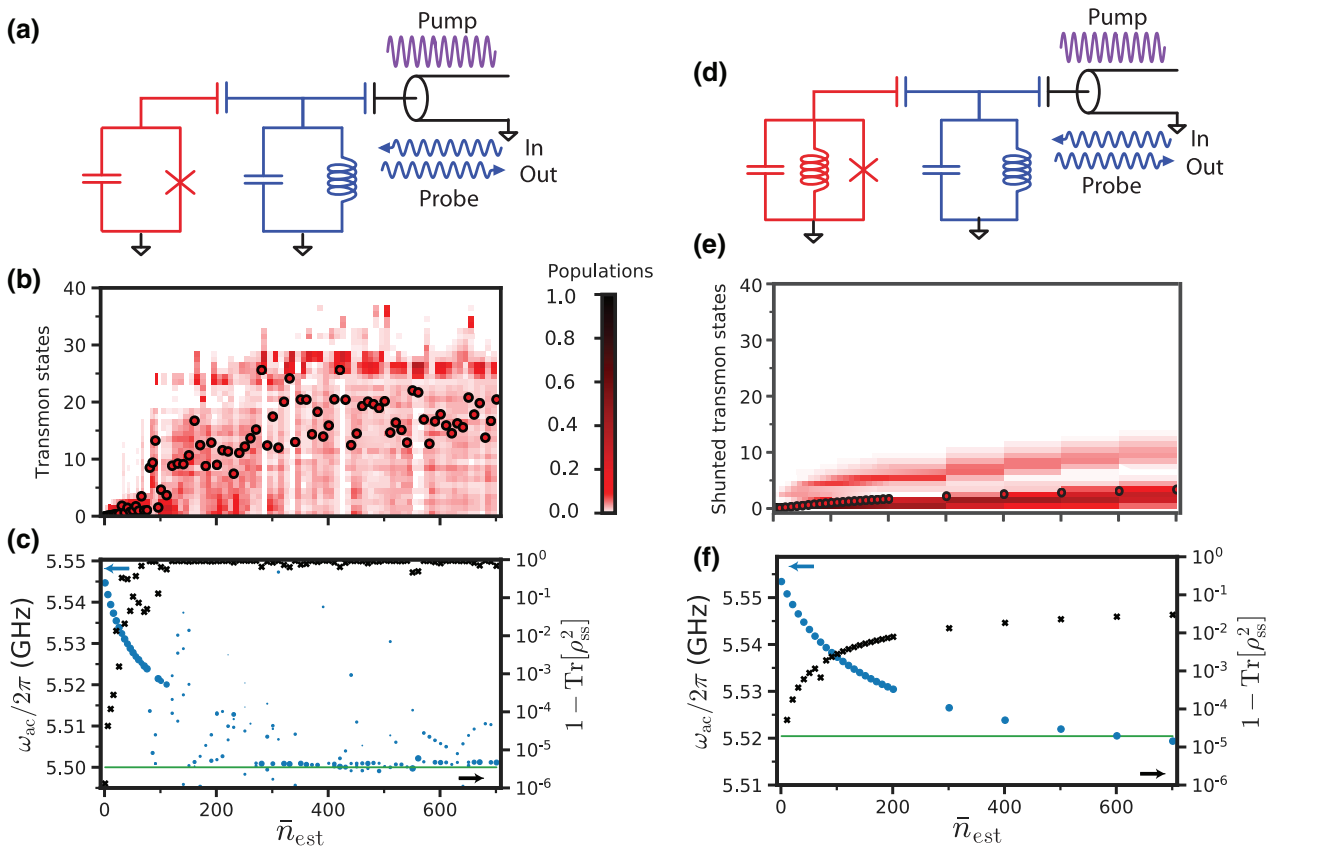


FIG. 1. Floquet-Markov simulations (asymptotic regime) of the unshunted and shunted transmon. (a),(d) The circuits of a regular transmon and an inductively shunted transmon, coupled to a harmonic oscillator and capacitively coupled to a transmission line. A (strong) off-resonant microwave drive at frequency $\omega_p$, called a pump, is sent to the system through the transmission line. (b),(e) The populations of the transmon eigenstates $|\eta_k\rangle$ and the shunted-transmon states $|\nu_k\rangle$ in the steady state $\rho_{ss}(0)$ of Eqs. (3)–(2) and of Eqs. (5)–(2), as a function of the pump power. In the unshunted case, the parameters are taken to be $E_C/h = 150$ MHz, $E_J/h = 20$ GHz, $g/2\pi = 140$ MHz, $\omega_a/2\pi = 5.5$ GHz, and $\omega_p/2\pi = 6$ GHz. For the shunted transmon, we use the same parameters except for $E_J/h = 6$ GHz and $E_L/h = 14$ GHz (leading to the same bare-transmon frequency). Here, $\bar{n}_{est} = |A_p|^2/4|\omega_p - \omega_a|^2$ is an estimation of the circulating photon number $\bar{n}$, where we use the bare oscillator frequency instead of the dressed one. The red dots indicate the average number of excitations in the transmon mode. (c),(f) The blue dots (left-hand axis) correspond to the ac Stark-shifted frequencies of the oscillator as a function of the pump power. The areas of the points are proportional to the associated transition probabilities (see Appendix B). The green horizontal line corresponds to the oscillator bare frequency $\omega_a$ in the unshunted case and to the renormalized frequency $\tilde{\omega}_a$ in the shunted one. In the first case, at many pump powers, we observe multiple resonance frequencies corresponding to different transitions from the limit cycle to Floquet states. In contrast, in the second one, the frequency is unique and well defined for all pump frequencies. This is also reflected by the impurity of the steady state (black crosses, right-hand axis). While, in the first case, the steady state is very mixed even for small pump strengths, in the second case, the impurity remains smaller than 3%.

For each pump power, we may observe a few resonance frequencies corresponding to various transitions and various Floquet states populated in the limit cycle. For weak drives $\bar{n} \ll 100$, we observe a linear behavior, in agreement with the usual ac Stark-shift experiments [21,22] and the associated theoretical work [25]. The behavior remains rather smooth up to $\bar{n} \approx 100$, with a slight curvature representing the effect of higher-order nonlinearities [26]. For $\bar{n} \gtrsim 300$, the dominant resonance frequency shifts near to the oscillator bare frequency. This can be physically understood by the fact that high-energy transmon states (energy above $2E_J$) are not affected by the cosine potential and therefore are well approximated by charge states. When reaching these levels [Fig. 1(b)], the transmon mode acts as a free particle (similar to the ionization of an atom), the dynamics of which follow that of the oscillator. The oscillator no longer inherits a nonlinearity from the transmon mode, as evidenced by the jump of its resonance frequency toward the bare frequency $\omega_a$. These two regimes slightly overlap in the middle region ($100 \lesssim \bar{n} \lesssim 300$), which presents many transition frequencies.

Previously, such a jump in the resonance frequency has been observed in a setup with a single strong probe drive and used to perform single-shot measurements of

the transmon qubit [13]. Various theoretical works have investigated this phenomenon, assuming two-level [27], multilevel [16,28,29], and Duffing approximations [30] of the transmon mode. In contrast to these approaches, the above numerical simulations of the full model given in Eqs. (3)–(2), and the experimental observations of [10], illustrate that such a jump in the resonance frequency coincides with the excitation of the transmon mode to high energy levels, well beyond the confinement potential.

## III. THE INDUCTIVELY SHUNTED TRANSMON: A SOLUTION TO INSTABILITY

The above analysis illustrates that in the parametric construction of a nonlinear Hamiltonian (such as the two-photon exchange between two modes), we are strongly limited in the span of the pump strength. Above a critical threshold, the ionized transmon no longer induces any nonlinearity on the oscillator. Such a limitation has been observed through the heating of the transmon mode in Ref. [9]. Further confinement of the nonlinear mode should provide a larger span of exploitable pump strength. We propose here to shunt the transmon circuit, with an inductance providing a harmonic confinement of the phase across the junction [31–33]. The Hamiltonian of such a circuit [shown in Fig. 1(d)] is given by

$$\begin{aligned}\mathbf{H}_{\text{shunt}}(t) = {} & \hbar\omega_a\,\mathbf{a}^\dagger\mathbf{a} + 4E_C\,\mathbf{N}^2 + \frac{E_L}{2}\,\boldsymbol{\varphi}^2 \\ & - E_J\cos(\boldsymbol{\varphi}) + i\hbar g\,\mathbf{N}\left(\mathbf{a}^\dagger - \mathbf{a}\right) \\ & + i\hbar\mathcal{A}_p(t)\left(\mathbf{a}^\dagger - \mathbf{a}\right), \end{aligned} \tag{4}$$

where $E_L$ is the shunt inductance energy and $\boldsymbol{\varphi}$ represents the dimensionless flux operator across the junction [18]. Previously, inductively shunted Josephson junctions have been considered as superconducting qubit designs [34,35]. Here, we consider parameters comparable to a flux qubit $E_C \ll E_J \lesssim E_L$. However, rather than the coherence properties of this circuit, we are interested in its behavior as a nonlinear device in the strong pumping regime. While at large numbers of excitations, the harmonic potential $(E_L/2)\,\boldsymbol{\varphi}^2$ dominates the nonlinear part $E_J\cos(\boldsymbol{\varphi})$, the passage to the linear regime should be smoother than with the transmon. We therefore expect to be able to explore the nonlinearity up to a higher number of excitations.

Similarly to the unshunted case, after a unitary transformation provided in Appendix A, the Hamiltonian of the inductively shunted transmon becomes

$$\begin{aligned}\tilde{\mathbf{H}}_{\text{shunt}}(t) = {} & \hbar\tilde{\omega}_a\,\tilde{\mathbf{a}}^\dagger\tilde{\mathbf{a}} + \hbar\tilde{\omega}_b\,\tilde{\mathbf{b}}^\dagger\tilde{\mathbf{b}} \\ & - E_J\cos\left[\varphi_a^0\left(\tilde{\mathbf{a}} + \tilde{\mathbf{a}}^\dagger\right) + \varphi_b^0\left(\tilde{\mathbf{b}} + \tilde{\mathbf{b}}^\dagger\right)\right. \\ & \left. + \xi\sin\left(\omega_p t\right)\right], \end{aligned} \tag{5}$$

where $\tilde{\omega}_a$ and $\tilde{\omega}_b$ are renormalized frequencies, $\varphi_a^0$ and $\varphi_b^0$ are zero-point fluctuations of the two modes as seen by the Josephson junction, and $\xi$ is a renormalized pump amplitude. Here, the mode $\tilde{\mathbf{a}}$ is closer to the initial oscillator mode $\mathbf{a}$ and the mode $\tilde{\mathbf{b}}$ is closer to the junction mode ($\varphi_a^0 \ll \varphi_b^0$). In contrast to the unshunted case, this change of variables ensures that both modes remain close to their ground state. This is a direct consequence of the harmonic confinement and will be confirmed through numerical simulations.

We again use the Floquet-Markov framework to carry out the numerical simulations of the driven dissipative system given in Eqs. (5) and (2). While the calculations are done in the basis of the Fock states of the two modes $\tilde{\mathbf{a}}$ and $\tilde{\mathbf{b}}$, we plot the results in the shunted-transmon basis $\{|\nu_k\rangle\}_{k=0}^{\infty}$ (eigenstates of the Hamiltonian $4E_C\mathbf{N}^2 + E_L\boldsymbol{\varphi}^2/2 - E_J\cos(\boldsymbol{\varphi})$). In Fig. 1(e), we plot the populations of the states $|\nu_k\rangle$ in the steady state together with the average number of excitations (red dots). We have not plotted the populations in mode $\tilde{\mathbf{a}}$, as it remains very close to its ground state. We observe that the state $\rho_{\text{ss}}(0)$ follows a very smooth behavior and, as shown in Fig. 1(f), the impurity of $\rho_{\text{ss}}$ (black crosses, right-hand axis) remains close to zero. As shown in Appendix B, in the frame corresponding to $\tilde{\mathbf{a}}$ and $\tilde{\mathbf{b}}$, this steady state remains very close to the ground state for all values of the pump power. Finally, Fig. 1(f) also illustrates the ac Stark-shifted frequency of the resonator mode, which is now well defined for all values of the pump power. The simulation parameters are chosen such that the bare frequencies, impedances, and coupling of the harmonic oscillator and the transmon mode coincide with those of the unshunted case. The important change concerns the dilution of the nonlinearity by the addition of the harmonic shunt with an energy $E_L$, about a factor of 2 larger than $E_J$ (for simulations with other parameters and comments on the choice of factor 2, see Appendix B).

As a result of this smooth behavior, we can extend the study to much higher pump powers. As illustrated in Fig. 2(a), the ac Stark-shifted frequency is well defined over a wide range of pump powers and exhibits a smooth oscillating behavior, decaying to $\tilde{\omega}_a$. This curve is in good agreement with the first-order predictions by a model resulting from time-averaging the Hamiltonian given in Eq. (5):

$$\begin{aligned}\tilde{\mathbf{H}}_{\text{av}} = {} & \hbar\tilde{\omega}_a\,\tilde{\mathbf{a}}^\dagger\tilde{\mathbf{a}} + \hbar\tilde{\omega}_b\,\tilde{\mathbf{b}}^\dagger\tilde{\mathbf{b}} \\ & - J_0(\xi)E_J\cos\left[\varphi_a^0\left(\tilde{\mathbf{a}} + \tilde{\mathbf{a}}^\dagger\right) + \varphi_b^0\left(\tilde{\mathbf{b}} + \tilde{\mathbf{b}}^\dagger\right)\right], \end{aligned} \tag{6}$$

where $J_0(\cdot)$ represents the Bessel function of the first kind. We note that the observed jump in the ac Stark shift of the unshunted case appears at pump strengths much lower than

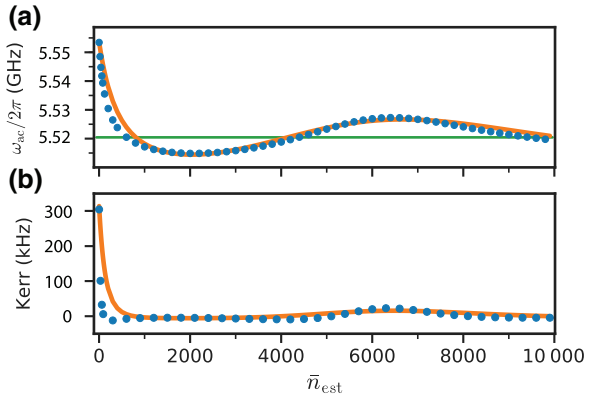


FIG. 2. (a) Floquet-Markov simulations of the ac Stark-shifted frequencies, for very large cavity photon numbers in the shunted case. The superimposed orange curve corresponds to the resonance frequency from the time-averaged model. Indeed, it is calculated as the difference between the two eigenenergies of the Hamiltonian given in Eq. (6) associated with the dressed $\tilde{\mathbf{a}}$-mode. The green line corresponds to the oscillator renormalized frequency $\tilde{\omega}_a$. (b) The strength of the induced Kerr effect of the most linear mode $\tilde{\mathbf{a}}$, defined as the difference of the transition frequencies for the first and the second excitations. The orange curve corresponds to the expected induced Kerr strength from the time-averaged model given in Eq. (6).

the first oscillation of this Bessel function. An experimental observation of such an oscillating behavior will prove a striking difference with the unshunted case.

This analysis indicates that we should also be able to tune the strength of various types of nonlinear Hamiltonians such as the induced Kerr effect of the mode $\tilde{\mathbf{a}}$ [3]. In Fig. 2(b), we plot the Kerr strength calculated from Floquet simulations (blue dots). Such a simulation is performed by determining the first and second excited Floquet states coupled to the ones in the limit cycle. Indeed, the Kerr strength is given by the difference of the transition frequencies for the first and second excitations. Interestingly, we observe that the Kerr term vanishes for sufficiently high powers. This ability to cancel the leading-order nonlinear effects by merely tuning a pump power will be an extremely useful tool for circuit QED experiments [36]. Furthermore, we plot the expected Kerr strength computed numerically from the time-averaged model given in Eq. (6) (orange curve). This is a first-order approximation of the Kerr effect and represents its qualitative behavior well. In order to achieve a more precise approximation, we need to perform higher-order rotating-wave approximations [37].

## IV. CONCLUSION

In summary, we investigate the nonlinear dissipative dynamics of a Josephson circuit in the presence of strong off-resonant drives. Drive and dissipation are central ingredients of many recent parametric protocols to engineer various linear or nonlinear Hamiltonians in the context of circuit QED. Through the analysis of the steady state of the driven system coupled to a cold bath, we demonstrate that the transmon circuit, commonly used for such a purpose, displays a structural instability in the exploitable range of pump powers. Indeed, even for moderate pump powers and a zero-temperature bath, this steady state is significantly mixed and is spanned by transmon states that are not confined in the cosine potential of the Josephson junction. The transmon states are progressively transformed into states acting as those of a free rotor, which do not induce any ac Stark shift of the oscillator. In contrast, shunting the transmon circuit with an appropriate inductance prevents the structural instability of the system and considerably increases the purity of its states. Therefore the nonlinearity of the Josephson junction can be exploited over a wide range of pump strengths. In particular, the induced Kerr effect can be canceled out with sufficiently high pump powers, while maintaining other signatures of nonlinearity. Finally, the Floquet-type analysis performed in this paper can be extended to other similar problems, such as the study of the dependence of the relaxation rate of a transmon qubit on the dispersive readout strength [15,38].

## ACKNOWLEDGMENTS

We gratefully acknowledge useful discussions with Steven Girvin, Leonid Glazman, Manuel Houzet, Benjamin Huard, Pierre Rouchon, and Alain Sarlette. This research was supported by the ANR grant ENDURANCE, the EMERGENCES grant ENDURANCE of Ville de Paris, by ARO under Grant No. W911NF-14-1-0011, and by Inria's DPEI under the TAQUILLA associated team.

## APPENDIX A: SIMULATED MODELS

### 1. The unshunted transmon

We start with the Hamiltonian of the circuit shown in Fig. 1(a):

$$\mathbf{H} = \hbar\omega_a\,\mathbf{a}^\dagger\mathbf{a} + 4E_C\left(\mathbf{N}-N_g\right)^2 - E_J\cos(\boldsymbol{\theta}) + i\hbar g\left(\mathbf{N}-N_g\right)\left(\mathbf{a}^\dagger-\mathbf{a}\right) + i\hbar\mathcal{A}_p(t)\left(\mathbf{a}^\dagger-\mathbf{a}\right), \quad \text{(A1)}$$

where $\omega_a$ is the frequency of the bare harmonic oscillator (in the absence of coupling to the transmon), $E_C$ and $E_J$ are the capacitive and Josephson energies of the transmon, and $g$ is the coupling strength. The pump is described by $\mathcal{A}_p(t) = A_p\cos(\omega_p t)$, where $A_p$ is the pump amplitude and $\omega_p$ is the pump frequency. Here, $\mathbf{N}$ and $\cos(\boldsymbol{\theta})$ are the transmon-mode operators corresponding to the number and transfer of Cooper pairs across the junction,

$$\begin{cases} \mathbf{N} = \sum_{N=-\infty}^{+\infty} |N\rangle\langle N|\,, \\ \cos(\boldsymbol{\theta}) = \frac{1}{2}\sum_{N=-\infty}^{+\infty} |N\rangle\langle N+1| + \text{H.c.}, \end{cases} \quad \text{(A2)}$$

and $\mathbf{a}$ is the cavity annihilation operator. Also, $N_g$ is the offset charge of the superconducting island. We model the dissipation as a capacitive coupling of the cavity to the transmission line provided by Eq. (2).

Let us displace the modes as $\tilde{\mathbf{a}} = \mathbf{a} - \bar{a}(t)$ and $\tilde{\boldsymbol{\theta}} = \boldsymbol{\theta} - \bar{\theta}(t)$, where

$$\bar{a}(t) = \frac{A_p}{2i}\left[\frac{e^{i\omega_p t}}{\omega_a + \omega_p} + \frac{e^{-i\omega_p t}}{\omega_a - \omega_p}\right],$$
$$\bar{\theta}(t) = \frac{2A_p g\omega_a}{\omega_p\left(\omega_a^2 - \omega_p^2\right)}\sin\left(\omega_p t\right) \mod (2\pi).$$

Note that here the displacement of $\boldsymbol{\theta}$ is equivalent to the application of a unitary given by $\mathbf{U} = \exp(i\bar{\theta}(t)\mathbf{N})$.

The Hamiltonian in the displaced frame is given by

$$\tilde{\mathbf{H}}(t) = \hbar\omega_a\,\tilde{\mathbf{a}}^\dagger\tilde{\mathbf{a}} + 4E_C\left(\mathbf{N} - N_g\right)^2 - E_J\cos[\tilde{\boldsymbol{\theta}} + \xi\sin(\omega_p t)] + i\hbar g\left(\mathbf{N} - N_g\right)\left(\tilde{\mathbf{a}}^\dagger - \tilde{\mathbf{a}}\right), \tag{A3}$$

where

$$\xi = \frac{2A_p g\omega_a}{\omega_p\left(\omega_a^2 - \omega_p^2\right)}.$$

This displacement brings the number of excitations in the harmonic oscillator close to zero. Additionally, it takes the pump drive into account as a drive on the superconducting phase of the transmon, inside the cosine term. These properties make the numerical simulations tractable.

At this point, one should note that under this change of variables, the coupling to the bath given in Eq. (2) is the same, using operators $\tilde{\mathbf{a}}^\dagger$ and $\tilde{\mathbf{a}}$ instead of $\mathbf{a}^\dagger$ and $\mathbf{a}$.

### 2. The inductively shunted transmon

The Hamiltonian of the circuit shown in Fig. 1(d) is given by

$$\mathbf{H}_{\text{shunt}}(t) = \hbar\omega_a\mathbf{a}^\dagger\mathbf{a} + 4E_C\mathbf{N}^2 + \frac{E_L}{2}\boldsymbol{\varphi}^2 - E_J\cos\boldsymbol{\varphi} + i\hbar g\,\mathbf{N}(\mathbf{a}^\dagger - \mathbf{a}) + i\hbar\mathcal{A}_p(t)(\mathbf{a}^\dagger - \mathbf{a}). \tag{A4}$$

This is similar to the Hamiltonian of the previous subsection, except for the additional term corresponding to the energy of the inductive shunt $E_L\boldsymbol{\varphi}^2/2$. Also, as a result of removing the superconducting island, and in contrast to the case of the previous subsection, the phase $\boldsymbol{\varphi}$ is no longer a compact variable and takes its values over the entire $\mathbb{R}$. This is why we use a different notation from the unshunted case: $\boldsymbol{\theta}$ denotes a phase defined in the compact interval $[0, 2\pi]$ and $\boldsymbol{\varphi}$ is a phase defined over the entire $\mathbb{R}$.

We start by defining $\mathbf{b} = (\boldsymbol{\varphi} + i\mathbf{N})/\sqrt{2}$. With the aim of diagonalizing the system and displacing it to take the drive into account, we perform, in order, a Bogoliubov transformation $\mathbf{U}_{s1}$, a beam-splitter-type unitary $\mathbf{U}_\theta$, a displacement of the frame $\mathbf{D}$, and another Bogoliubov transformation $\mathbf{U}_{s2}$, given by

$$\mathbf{U}_{s1} = \exp\left[\frac{\zeta}{2}(\mathbf{b}^{\dagger 2} - \mathbf{b}^2)\right],$$
$$\mathbf{U}_\theta = \exp[\theta(\mathbf{a}\mathbf{b}^\dagger - \mathbf{a}^\dagger\mathbf{b})],$$
$$\mathbf{D} = \exp[\alpha^*(t)\mathbf{a} - \alpha(t)\mathbf{a}^\dagger]\exp[\beta^*(t)\mathbf{b} - \beta(t)\mathbf{b}^\dagger],$$
$$\mathbf{U}_{s2} = \exp\left[\frac{\zeta_a}{2}(\mathbf{a}^{\dagger 2} - \mathbf{a}^2)\right]\exp\left[\frac{\zeta_b}{2}(\mathbf{b}^{\dagger 2} - \mathbf{b}^2)\right].$$

Here,

$$\theta = -\frac{1}{2}\arctan\left[\frac{2\hbar g\sqrt{2E_L\hbar\omega_a}}{(\hbar\omega_a)^2 - 8E_C E_L}\right],$$
$$\alpha(t) = \frac{A_p\cos\theta}{\omega_p^2 - \omega_a\omega_1}\left[\omega_p\sin(\omega_p t) + i\omega_a\cos(\omega_p t)\right],$$
$$\beta(t) = \frac{A_p\sin\theta}{\omega_p^2 - \omega_a\omega_2}\left[\omega_p\sin(\omega_p t) + i\omega_a\cos(\omega_p t)\right],$$
$$\zeta = \log\left(\sqrt{\frac{E_L}{\hbar\omega_a}}\right),$$
$$\zeta_a = \log\left(\sqrt[4]{\frac{\omega_a}{\omega_1}}\right), \quad \zeta_b = \log\left(\sqrt[4]{\frac{\omega_a}{\omega_2}}\right),$$

with

$$\omega_1 = \omega_a\cos^2\theta + \frac{8E_C E_L}{\hbar^2\omega_a}\sin^2\theta - g\sqrt{\frac{2E_L}{\hbar\omega_a}}\sin(2\theta),$$
$$\omega_2 = \omega_a\sin^2\theta + \frac{8E_C E_L}{\hbar^2\omega_a}\cos^2\theta + g\sqrt{\frac{2E_L}{\hbar\omega_a}}\sin(2\theta).$$

This leads to a Hamiltonian given by

$$\tilde{\mathbf{H}}_{\text{shunt}}(t) = \hbar\tilde{\omega}_a\tilde{\mathbf{a}}^\dagger\tilde{\mathbf{a}} + \hbar\tilde{\omega}_b\tilde{\mathbf{b}}^\dagger\tilde{\mathbf{b}} - E_J\cos\left[\phi_a(\tilde{\mathbf{a}}^\dagger + \tilde{\mathbf{a}}) + \phi_b(\tilde{\mathbf{b}}^\dagger + \tilde{\mathbf{b}}) + \xi\sin(\omega_p t)\right], \tag{A5}$$

where

$$\tilde{\omega}_a = \sqrt{\omega_a\omega_1}, \quad \tilde{\omega}_b = \sqrt{\omega_a\omega_2},$$
$$\phi_a = -\sin(\theta)\sqrt{\frac{\hbar\omega_a}{2E_L}}\sqrt[4]{\frac{\omega_1}{\omega_a}}, \quad \phi_b = \cos(\theta)\sqrt{\frac{\hbar\omega_a}{2E_L}}\sqrt[4]{\frac{\omega_2}{\omega_a}},$$
$$\xi = A_p\omega_p\sin(2\theta)\sqrt{\frac{\hbar\omega_a}{2E_L}}\left(\frac{1}{\omega_p^2 - \omega_a\omega_2} - \frac{1}{\omega_p^2 - \omega_a\omega_1}\right).$$

Under this change of variables, the coupling to the bath given in Eq. (2), through the operator $i(\mathbf{a} - \mathbf{a}^\dagger)$, is

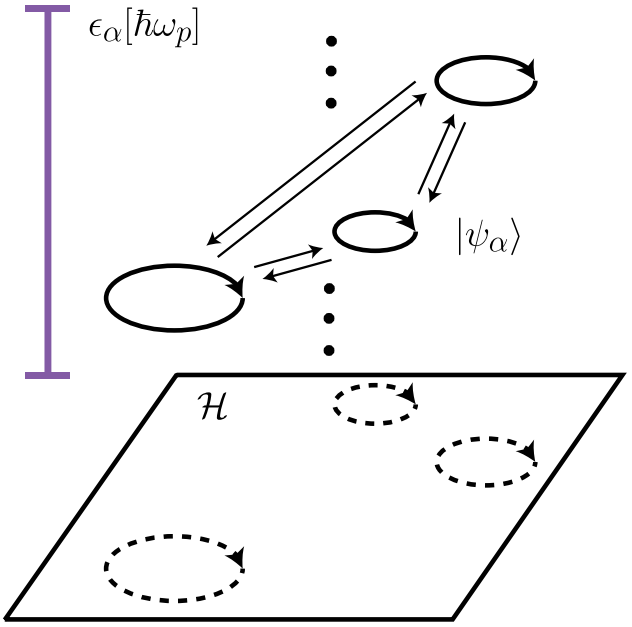


FIG. 3. Driven-dissipative quantum circuits and the Floquet-Markov theory. The Floquet states $\{|\Psi_\alpha(t)\rangle\}_\alpha$ are periodic orbits of the driven system in its Hilbert space $\mathcal{H}$. A quasienergy $\epsilon_\alpha$ is associated with each Floquet state $|\Psi_\alpha(t)\rangle$. The set of quasienergies is invariant under translation by multiples of $\hbar\omega_p$ (different Brillouin zones). Here, we plot the Floquet states of the first Brillouin zone (with quasienergies defined modulo $\hbar\omega_p$ and denoted by $\epsilon_\alpha[\hbar\omega_p]$) and their transitions due to the coupling to the bath. The steady state of the driven-dissipative system is given by a statistical mixture of these Floquet states, with populations inferred from an extension of the Fermi golden rule.

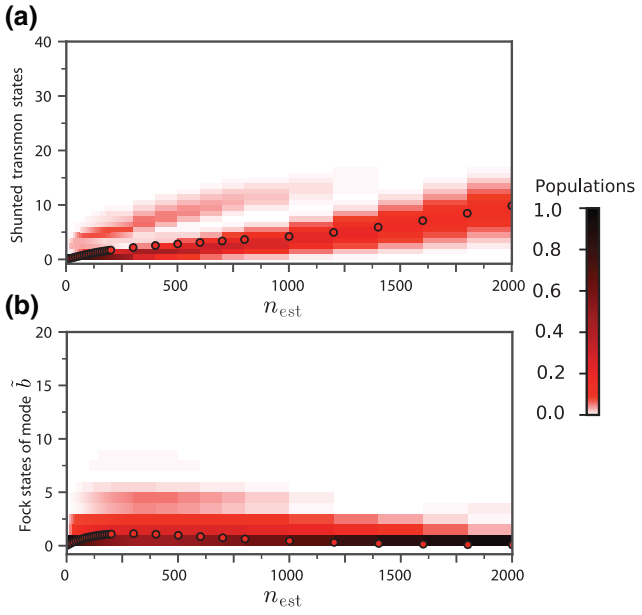


FIG. 4. Floquet-Markov simulations (asymptotic regime) of Eqs. (A5)–(A6) with $E_C/h = 150$ MHz, $E_J/h = 6$ GHz, $E_L/h = 14$ GHz, $g/2\pi = 140$ MHz, $\omega_a/2\pi = 5.5$ MHz, and $\omega_p/2\pi = 6$ GHz. (a) The populations of the shunted-transmon eigenstates $|\nu_k\rangle$ in the steady state $\rho_{\rm ss}(0)$ as a function of the pump power. (b) The populations of the $\tilde{\mathbf{b}}$-mode's Fock states in the same steady state.

replaced by

$$\nu = i\cos(\theta)\sqrt[4]{\frac{\omega_1}{\omega_a}}(\tilde{\mathbf{a}} - \tilde{\mathbf{a}}^\dagger) + i\sin(\theta)\sqrt[4]{\frac{\omega_2}{\omega_a}}(\tilde{\mathbf{b}} - \tilde{\mathbf{b}}^\dagger).$$

Therefore, the new system-bath coupling is given by

$$\begin{aligned}\tilde{\mathbf{H}_{SB}} = &\sum_k \hbar\omega_k \mathbf{c}^\dagger[\omega_k]\mathbf{c}[\omega_k] \\ &- \hbar\Omega[\omega_k]\cos(\theta)\sqrt[4]{\frac{\omega_1}{\omega_a}}(\tilde{\mathbf{a}}^\dagger - \tilde{\mathbf{a}})(\mathbf{c}^\dagger[\omega_k] - \mathbf{c}[\omega_k]) \\ &- \hbar\Omega[\omega_k]\sin(\theta)\sqrt[4]{\frac{\omega_2}{\omega_a}}(\tilde{\mathbf{b}}^\dagger - \tilde{\mathbf{b}})(\mathbf{c}^\dagger[\omega_k] - \mathbf{c}[\omega_k]).\end{aligned} \tag{A6}$$

## APPENDIX B: FLOQUET SIMULATIONS

### 1. The Hamiltonian formulation of the Floquet theory

We consider here a system evolving under a time-periodic Hamiltonian $\tilde{H}(t)$, of period $T = 2\pi/\omega_p$. Such a system can be efficiently simulated using the tools from the Floquet theory [[17], Section 2]. In this section, we recall some of the basic elements of the Floquet theory that are required to understand the simulations of this paper. This material is borrowed and summarized from [17].

The Schrödinger equation for this system is

$$i\hbar\frac{\partial}{\partial t}\left|\tilde{\Psi}(t)\right\rangle = \tilde{\mathbf{H}}(t)\left|\tilde{\Psi}(t)\right\rangle, \tag{B1}$$

where $\left|\tilde{\Psi}(t)\right\rangle$ denotes the state of the system at time $t$. The Floquet theorem states that there exist solutions to Eq. (B1) of the form

$$|\Psi_{\tilde{\alpha}}(t)\rangle = e^{-i\epsilon_{\tilde{\alpha}}t/\hbar}\,|\Phi_{\tilde{\alpha}}(t)\rangle\,, \tag{B2}$$

where $|\Phi_{\tilde{\alpha}}\rangle$ is called a *Floquet mode* and is $T$-periodic in time and $\epsilon_{\tilde{\alpha}}$ is a real-valued energy, called a *quasienergy*. In particular, we note that the set of quasienergies is invariant under translation by multiples of $\hbar\omega_p$, as for any Floquet mode $|\Phi_{\tilde{\alpha}}(t)\rangle$, the periodic wave function $\exp(in\omega_p t)\,|\Phi_{\tilde{\alpha}}(t)\rangle$ is also a Floquet mode. Therefore, the index $\tilde{\alpha}$ corresponds to two indices $(\alpha, n) \in [-\hbar\omega_p/2, \hbar\omega_p/2[\times\mathbb{Z}$, with $\epsilon_{\alpha,n} = \epsilon_\alpha + n\omega_p$. Each value of $n$ here corresponds to a Brillouin zone. In this appendix, we consider the first Brillouin zone $(\alpha, 0)$, which we replace by $\alpha$ to simplify the notation.

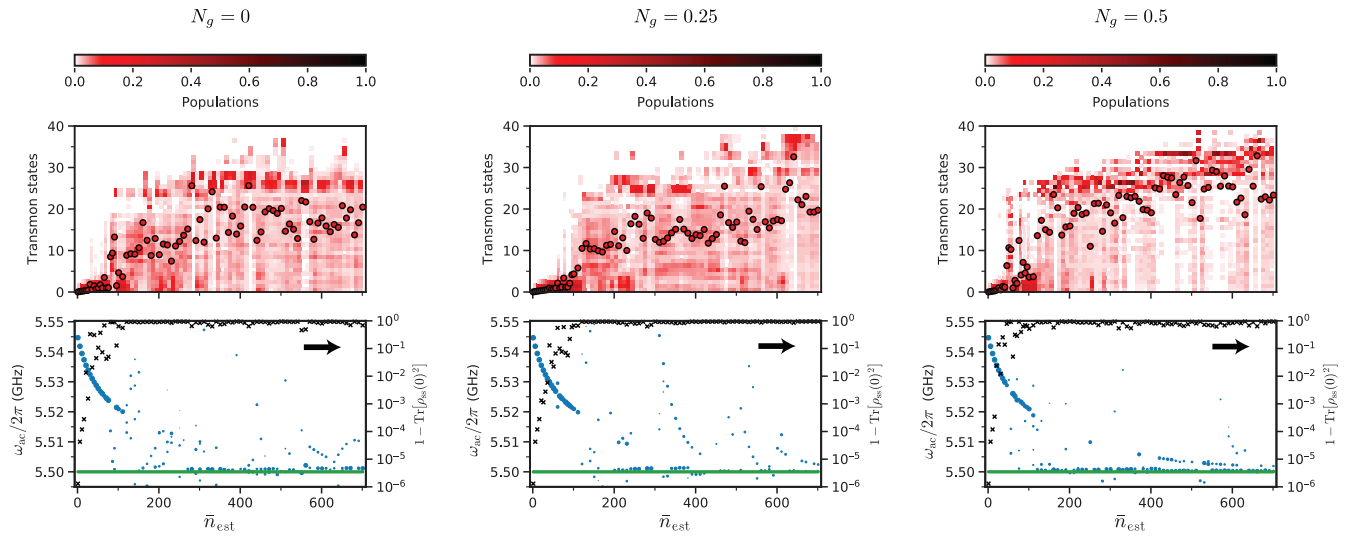


FIG. 5. Floquet-Markov simulations (in the asymptotic regime) of Eqs. (A1)–(2), using the same parameters as in Sec. II and three different values of $N_g$. In the upper figures, we plot the populations of the transmon eigenstates in the steady state $\rho_{ss}(0)$ as a function of the pump power. Also, the red dots indicate the average number of excitations in the transmon mode. In the lower figures, we plot the ac Stark-shifted frequencies of the oscillator (blue dots) and the impurity of the steady state (black crosses, right-hand axis) as a function of the pump power. As can be seen, we observe no significant qualitative differences between the three cases. The steady state rapidly becomes very mixed and highly excited and the frequency is not well defined for $\bar{n}$ larger than 100.

A general approach to solving the above Schrödinger equation is to identify the Floquet modes and the associated quasienergies. By decomposing the initial state as a superposition of the Floquet modes of the first Brillouin zone at time $t = 0$, $|\Psi(0)\rangle = \sum_\alpha c_\alpha |\Phi_\alpha(0)\rangle$, the solution at time $t$ is given by

$$|\Psi(t)\rangle = \sum_\alpha c_\alpha e^{-i\epsilon_\alpha t/\hbar} |\Phi_\alpha(t)\rangle .$$

In order to identify the Floquet modes and the quasienergies, we note that by applying the propagator $\tilde{\mathbf{U}}(t+T,t)$ of Eq. (B1) to a Floquet solution, we obtain

$$\tilde{\mathbf{U}}(t+T,t)\,|\Phi_\alpha(t)\rangle = e^{-i\epsilon_\alpha T/\hbar}\,|\Phi_\alpha(T+t)\rangle \tag{B3}$$

and in particular, at $t = 0$,

$$\tilde{\mathbf{U}}(T,0)\,|\Phi_\alpha(0)\rangle = e^{-i\epsilon_\alpha T/\hbar}\,|\Phi_\alpha(0)\rangle . \tag{B4}$$

Equation (B4) can be used to numerically compute the Floquet modes at $t = 0$ and their quasienergies through the eigenstates and eigenvalues of $\tilde{\mathbf{U}}(T,0)$. Then, we can obtain the value of the Floquet mode at any later time using

$$|\Phi_\alpha(t)\rangle = e^{i\epsilon_\alpha t/\hbar}\tilde{\mathbf{U}}(t,0)\,|\Phi_\alpha(0)\rangle . \tag{B5}$$

### 2. The Floquet-Markov approach for weak dissipation

The Floquet theory can be extended to take weak dissipations into account. Under the Floquet-Markov-Born approximation [[17], Section 9], one can write a master equation in the basis of the Floquet modes of the first Brillouin zone:

$$\begin{aligned}\dot{\rho}_{\alpha\alpha}(t) &= \sum_\nu \left[L_{\alpha\nu}\rho_{\nu\nu}(t) - L_{\nu\alpha}\rho_{\alpha\alpha}(t)\right],\\ \dot{\rho}_{\alpha\beta}(t) &= -\frac{1}{2}\sum_\nu \left(L_{\nu\alpha} + L_{\nu\beta}\right)\rho_{\alpha\beta}(t), \quad \alpha \neq \beta,\end{aligned} \tag{B6}$$

where $\left(\rho_{\alpha\beta}\right) = \langle\Phi_\alpha(t)|\,\rho\,\left|\Phi_\beta(t)\right\rangle$ are the components of the density matrix $\rho$. We have defined

$$L_{\alpha\beta} = \sum_{k=-\infty}^{+\infty}\left[\gamma_{\alpha,\beta,k} + n_{\mathrm{th}}(|\Delta_{\alpha,\beta,k}|)\left(\gamma_{\alpha,\beta,k} + \gamma_{\beta,\alpha,-k}\right)\right]. \tag{B7}$$

Here,

$$\gamma_{\alpha,\beta,k} = 2\pi\,\Theta\left(\Delta_{\alpha\beta k}\right)J\left(\Delta_{\alpha,\beta,k}\right)\left|P_{\alpha\beta k}\right|^2, \tag{B8}$$

where $\Theta$ is the Heaviside distribution, $\hbar\Delta_{\alpha,\beta,k} = \epsilon_\beta - \epsilon_\alpha + k\hbar\omega_p$ is a quasienergy difference, and $J(\omega)$ is the noise-spectral function of the environmental coupling. The matrix elements, $P_{\alpha\beta k}$, are given by

$$P_{\alpha\beta k} = \frac{i}{T}\int_0^T e^{-ik\omega_p t}\,\langle\Phi_\alpha(t)|\,(\tilde{\mathbf{a}} - \tilde{\mathbf{a}}^\dagger)\,\left|\Phi_\beta(t)\right\rangle\,dt. \tag{B9}$$

Finally, $n_{\mathrm{th}}(\omega) = 1/[\exp(\hbar\omega/k_BT) - 1]$ is the thermal occupation of the bath at frequency $\omega$. In our simulations, we assume a zero temperature and therefore $n_{\mathrm{th}} \equiv 0$.

Under some nondegeneracy assumptions (absence of resonance), the steady state of Eq. (B6) is diagonal in the Floquet-modes basis. Moreover, the diagonal of this steady-state density matrix can be numerically computed by solving the linear system $Rp = 0$, where $(p_\alpha)_\alpha = (\rho_{\alpha\alpha})_\alpha$ is the diagonal of the steady-state density matrix and $\left(R_{\alpha\beta}\right)_{\alpha\beta} = \left(L_{\alpha\beta} - \delta_{\alpha\beta}\sum_\nu L_{\alpha\nu}\right)_{\alpha\beta}$, with $\delta_{\alpha\beta}$ being the Kronecker delta.

### 3. The numerical calculation of steady states

The steady states in the simulations of Figs. 1(b) and 1(e) have been numerically calculated following the above approach. We start by computing the Floquet modes and then we reconstruct the stochastic transition matrix $R$. After calculating the steady states as statistical mixtures of the Floquet modes, we plot them in an appropriate basis of the Hilbert space. All our numerical simulations are run on a desktop workstation with an Intel Core i7-6700 processor. We are running our simulations on a modified version of Qutip 4.2.0 [39,40] under Python 3.5.2 and the plots have been produced using MATPLOTLIB [41]. In the unshunted case, and in the displaced frame provided in Appendix 1, we require a truncation of about 50 transmon states and ten oscillator Fock states. For the unshunted case, we go to a frame provided in Appendix 2. As a result of the stable behavior in this case, we require a smaller truncation of about 20 Fock states of the nonlinear mode and ten Fock states of the linear one.

In Fig. 1(e), in order to put the system in a similar basis as in Fig. 1(b) for the unshunted case, we plot the steady states in the shunted-transmon basis after applying the inverse of the unitary transformations of Appendix 2. Here, in Fig. 4, we provide this steady state over an extended span of pump powers, and both in the shunted-transmon basis $|\nu_k\rangle$ of $4E_C\mathbf{N}^2 + E_L\boldsymbol{\varphi}^2/2 - E_J\cos(\boldsymbol{\varphi})$ and in the distorted, rotated, and displaced frame $\tilde{\mathbf{a}}$ and $\tilde{\mathbf{b}}$, of Appendix 2. We see that in this second frame, the steady state remains very close to the ground state of the mode $\tilde{\mathbf{b}}$, for all values of the pump power. This statement is also true for the mode $\tilde{\mathbf{a}}$.

### 4. The computation of ac Stark shifts

We are interested in the resonance frequency of the driven system with Hamiltonian $\tilde{H}(t)$, close to the oscillator's bare frequency. Experimentally, we can find such a resonance frequency by sweeping the frequency of a very weak probe drive around the oscillator's frequency [10]. We model this weak probe as a small perturbative Hamiltonian $i\hbar\varepsilon(t)\left(\tilde{\mathbf{a}}^\dagger - \tilde{\mathbf{a}}\right)$.

As shown in previous subsections, the system converges asymptotically to a limit cycle given by a statistical mixture of Floquet states:

$$\rho_{\rm ss}(t) = \sum_\alpha p_\alpha \left|\Phi_\alpha(t)\right\rangle \left\langle\Phi_\alpha(t)\right| .$$

Initializing the system at one of the Floquet modes $|\Phi_\alpha\rangle$ populated in the steady state, let us focus on the solution of the Schrödinger equation in the presence of the weak probe. We consider this solution at the lowest order in the amplitude of the probe field. In this case, the Schrödinger equation is

$$\frac{\partial}{\partial t}\left|\Psi(t)\right\rangle = -\frac{i}{\hbar}\mathbf{H}_\varepsilon(t)\left|\Psi(t)\right\rangle , \;\; \left|\Psi(0)\right\rangle = \left|\Phi_\alpha(0)\right\rangle , \tag{B10}$$

where $\mathbf{H}_\varepsilon(t) = \tilde{\mathbf{H}}(t) + i\varepsilon(t)\left(\tilde{\mathbf{a}}^\dagger - \tilde{\mathbf{a}}\right)$.

First, let us introduce the propagation operator $\tilde{\mathbf{U}}(t,0)$ associated with the $\tilde{\mathbf{H}}(t)$ Hamiltonian:

$$\frac{\partial\tilde{\mathbf{U}}(t,0)}{\partial t} = -\frac{i}{\hbar}\tilde{\mathbf{H}}(t)\tilde{\mathbf{U}}(t,0), \quad \tilde{\mathbf{U}}(0,0) = \mathbf{I}.$$

The solution of Eq. (B10) is given by

$$\begin{aligned}\left|\Psi(t)\right\rangle &= \tilde{\mathbf{U}}(t,0)\left|\Phi_\alpha(0)\right\rangle \\ &\quad + \frac{1}{\hbar}\tilde{\mathbf{U}}(t,0)\int_0^t \varepsilon(s)\tilde{\mathbf{U}}(s,0)^\dagger\left(\tilde{\mathbf{a}}^\dagger - \tilde{\mathbf{a}}\right)\tilde{\mathbf{U}}(s,0) \\ &\times\left|\Phi_\alpha(0)\right\rangle\, ds \\ &= e^{-i\epsilon_\alpha t/\hbar}\left|\Phi_\alpha(t)\right\rangle \\ &\quad + \frac{1}{\hbar}\tilde{\mathbf{U}}(t,0)\int_0^t \varepsilon(s)e^{-i\epsilon_\alpha s/\hbar}\tilde{\mathbf{U}}(s,0)^\dagger \\ &\quad \times\left(\tilde{\mathbf{a}}^\dagger - \tilde{\mathbf{a}}\right)\left|\Phi_\alpha(s)\right\rangle\, ds. \end{aligned} \tag{B11}$$

Let us now focus on the overlap of $|\Psi(t)\rangle$ with other Floquet modes $\left|\Phi_\beta(t)\right\rangle$. We have, from Eq. (B11),

$$\begin{aligned}\left\langle\Phi_\beta(t)\right|\left.\Psi(t)\right\rangle &= e^{-i\epsilon_\alpha t/\hbar}\left\langle\Phi_\beta(t)\right|\left.\Phi_\alpha(t)\right\rangle \\ &\quad + \frac{1}{\hbar}\left\langle\Phi_\beta(t)\right|\tilde{\mathbf{U}}(t,0)\int_0^t \varepsilon(s)e^{-i\epsilon_\alpha s/\hbar}\tilde{\mathbf{U}}(s,0)^\dagger \\ &\quad \times\left(\tilde{\mathbf{a}}^\dagger - \tilde{\mathbf{a}}\right)\left|\Phi_\alpha(s)\right\rangle\, ds, \end{aligned} \tag{B12}$$

that is,

$$\begin{aligned}\left\langle\Phi_\beta(t)\right|\left.\Psi(t)\right\rangle &= e^{-i\epsilon_\alpha t/\hbar}\left\langle\Phi_\beta(t)\right|\left.\Phi_\alpha(t)\right\rangle \\ &\quad + \frac{1}{\hbar}e^{-i\epsilon_\beta t/\hbar}\int_0^t \varepsilon(s)e^{i(\epsilon_\beta-\epsilon_\alpha)s/\hbar}\left\langle\Phi_\beta(s)\right| \\ &\quad \times\left(\tilde{\mathbf{a}}^\dagger - \tilde{\mathbf{a}}\right)\left|\Phi_\alpha(s)\right\rangle\, ds \\ &= e^{-i\epsilon_\alpha t/\hbar}\left\langle\Phi_\beta(t)\right|\left.\Phi_\alpha(t)\right\rangle \\ &\quad - \frac{i}{\hbar}e^{-i\epsilon_\beta t/\hbar}\sum_k\int_0^t \varepsilon(s)e^{i\Delta_{\alpha,\beta,k}s}P_{\beta,\alpha,k}ds. \end{aligned}$$

To induce a transition in the system between the Floquet modes $|\Phi_\alpha\rangle$ and $|\Phi_\beta\rangle$, one needs the frequency of the probe drive $\varepsilon(t)$ to match one of the frequencies $\Delta_{\alpha,\beta,k}$ and, furthermore, that the associated matrix element $P_{\beta,\alpha,k}$ is nonzero. Moreover, the transition rate is proportional to both the population of the initial Floquet mode $|\Phi_\alpha\rangle$ in the steady state $\rho_{\rm ss}$, given by $p_\alpha$, and the matrix element $P_{\beta,\alpha,k}$. In Figs. 1(c) and 1(f), we plot the predominant transition frequencies at each pump power.

### 5. The unshunted transmon and charge offset

In this subsection, we focus on the unshunted case and study the effect of the charge offset $N_g$. In the simulations of Sec. II, we take $N_g = 0$. As we can see in Fig. 5, the choice of $N_g$ in the Hamiltonian given in Eq. (A1) does not have any significant effect on the qualitative behavior of the system in the steady state.

### 6. The choice of parameters for the shunted transmon

The simulations of Sec. III are performed with the same parameters as in the unshunted case, except for the Josephson energy, which is taken to be $E_J/h = 6$ GHz, and the addition of $E_L/h = 14$ GHz. Noting that the sum of these two energies corresponds to the Josephson energy in the unshunted case, this choice allows us to keep the bare frequency of the transmon mode the same. This, however, comes at the expense of diluting the nonlinearity of the transmon mode. Indeed, the anharmonicity of the shunted-transmon mode is given by 37 MHz, to be compared to 143 MHz in the unshunted case. In the same way, the induced Kerr effect on the cavity of 306 kHz is weaker than 655 kHz for the unshunted case. The shallower slope of the ac Stark shift in Fig. 1(f) [with respect to Fig. 1(c)] can be explained by means of this difference.

Using a different set of parameters, one can achieve similar nonlinearities for the shunted transmon. For instance, by choosing $E_C/h = 450$ MHz, $E_J/h = 2.22$ GHz, $E_L/h = 4.44$ GHz, $g/2\pi = 245$ MHz, and $\omega_a = 5.5$ GHz, we achieve similar frequencies and nonlinearities to the shunted case. More precisely, in the absence of the pump, we find the cavity frequency to be 5.545 GHz, the qubit frequency to be 4.7 GHz, the qubit anharmonicity to be 123 MHz, the induced cavity Kerr effect to be 600 kHz, and the cross-Kerr effect between the qubit and the cavity to be 15.5 MHz. These parameters for the unshunted case are given, respectively, by 5.545 GHz, 4.691 GHz, 143 MHz, 655 kHz, and 17.3 MHz. In Fig. 6(a), we plot and compare the shifted cavity frequencies in the shunted and unshunted cases (blue dots, left-hand axis). The slope near $\bar{n}_{\rm est} = 0$ of the variation of frequency versus the photon number $\bar{n}_{\rm est}$ is now very close to that of the unshunted case. We also plot the impurity of the steady state in both cases versus the pump power (black and gray crosses, right-hand axis). One clearly observes a much purer and smoother behavior for the shunted case with respect to the unshunted one. In Figs. 6(b) and 6(c), we plot the shifted cavity frequency and induced Kerr effect over a larger range of pump powers for the shunted case with these new parameters. We observe a behavior similar to that shown in panels (a) and (b) of Fig. 2. As a result of the increased nonlinearity, the range of values taken by the Kerr strength is twice as large as in the simulations of the shunted case with the parameters in Sec. III.

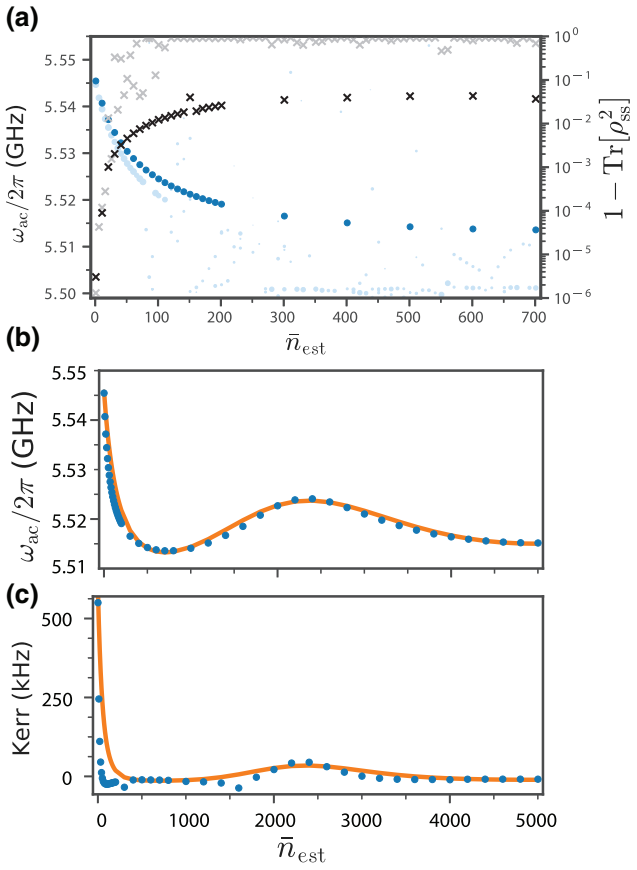


FIG. 6. Floquet-Markov simulations of the shunted transmon with parameters $E_C/h = 450$ MHz, $E_J/h = 2.22$ GHz, $E_L/h = 4.44$ GHz, $g/2\pi = 245$ MHz, $\omega_a/2\pi = 5.5$ GHz, and $\omega_p/2\pi = 6$ GHz. (a) The blue dots correspond to the ac Stark-shifted frequencies of the oscillator as a function of the pump power. For comparison, we have also reproduced the results for the unshunted case with the parameters of Fig. 1. These are plotted as pale blue dots (left-hand axis). We also have plotted the impurity of the steady state (black crosses, right-hand axis) versus the corresponding results for the unshunted case (gray crosses, right-hand axis). (b) We plot the ac Stark-shifted frequency with the shunted transmon over an extended range of pump powers. The blue dots correspond to the Floquet simulation results and the orange curve indicates the expected values from a time-averaged model. This is to be compared to Fig. 2(a). (c) The induced Kerr strength over the same extended range [to be compared with Fig. 2(b)].

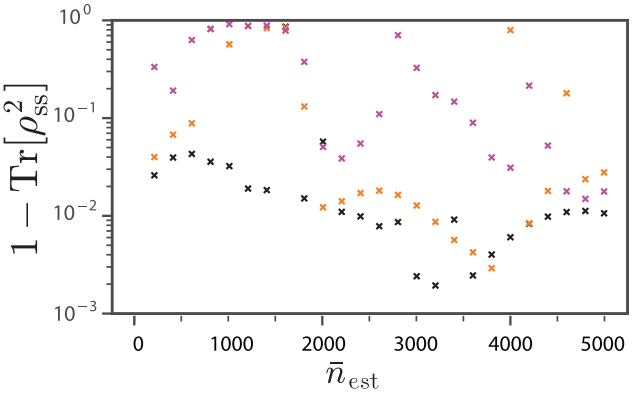


FIG. 7. The impurity of the steady state as a function of the pump power. We use the same parameters as in Fig. 6, except for $E_J$ and $E_L$. While the sum $(E_J + E_L)/h = 6.66$ GHz is fixed, we take three different choices for their ratio $r = E_L/E_J$. The black crosses correspond to $r = 2$ ($E_L/h = 4.44$ GHz and $E_J/h = 2.22$ GHz), the orange ones to $r = 1.5$ ($E_L/h = 4$ GHz and $E_J/h = 2.22$ GHz), and the magenta ones to $r = 1$ ($E_L/h = E_J/h = 3.33$ GHz).

In these simulations, similar to the previous set of parameters, we have chosen a ratio between $E_L$ and $E_J$ of about 2. Noting that a large ratio between $E_L$ and $E_J$ leads to the dilution of the nonlinearity of the Josephson junctions, one may consider the possibility of choosing a smaller ratio. We will see, however, that this comes at the expense of losing the purity of the steady state and therefore getting closer to the asymptotic behavior in the unshunted case. In order to illustrate this, we perform numerical simulations with the same parameters as in Fig. 6, except for $E_J$ and $E_L$. Indeed, we fix their sum $(E_J + E_L)/h = 6.66$ GHz and we let the ratio between them vary. In Fig. 7, we provide the impurity of the steady state as a function of the pump power for three different choices of the ratio $r = E_L/E_J$. As can be seen, a ratio of 2, as chosen in this paper, ensures globally a purer steady state and this purity is lost for smaller ratios.


[1] A. Wallraff, D. I. Schuster, A. Blais, L. Frunzio, R.-S. Huang, J. Majer, S. Kumar, S. M. Girvin, and R. J. Schoelkopf, Strong coupling of a single photon to a superconducting qubit using circuit quantum electrodynamics, Nature **431**, 162 (2004).

[2] D. I. Schuster, A. A. Houck, J. A. Schreier, A. Wallraff, J. M. Gambetta, A. Blais, L. Frunzio, J. Majer, B. Johnson, M. H. Devoret, S. M. Girvin, and R. J. Schoelkopf, Resolving photon number states in a superconducting circuit, Nature **445**, 515 (2007).

[3] Gerhard Kirchmair, Brian Vlastakis, Zaki Leghtas, Simon E. Nigg, Hanhee Paik, Eran Ginossar, Mazyar Mirrahimi, Luigi Frunzio, S. M. Girvin, and R. J. Schoelkopf, Observation of quantum state collapse and revival due to the single-photon Kerr effect, Nature **495**, 205 (2013).

[4] Baleegh Abdo, Katrina Sliwa, Flavius Schackert, Nicolas Bergeal, Michael Hatridge, Luigi Frunzio, A. Douglas Stone, and Michel Devoret, Full Coherent Frequency Conversion Between Two Propagating Microwave Modes, Phys. Rev. Lett. **110**, 173902 (2013).

[5] M. A. Castellanos-Beltran, K. D. Irwin, G. C. Hilton, L. R. Vale, and K. W. Lehnert, Amplification and squeezing of quantum noise with a tunable Josephson metamaterial, Nat. Phys. **4**, 929 (2008).

[6] E. Flurin, N. Roch, F. Mallet, M. H. Devoret, and B. Huard, Generating Entangled Microwave Radiation over Two Transmission Lines, Phys. Rev. Lett. **109**, 183901 (2012).

[7] U. Vool, S. Shankar, S. O. Mundhada, N. Ofek, A. Narla, K. Sliwa, E. Zalys-Geller, Y. Liu, L. Frunzio, R. J. Schoelkopf, S. M. Girvin, and M. H. Devoret, Continuous Quantum Nondemolition Measurement of the Transverse Component of a Qubit, Phys. Rev. Lett. **117**, 133601 (2016).

[8] Z. Leghtas, S. Touzard, I. M. Pop, A. Kou, B. Vlastakis, A. Petrenko, K. M. Sliwa, A. Narla, S. Shankar, M. J. Hatridge, M. Reagor, L. Frunzio, R. J. Schoelkopf, M. Mirrahimi, and M. H. Devoret, Confining the state of light to a quantum manifold by engineered two-photon loss, Science **347**, 853 (2015).

[9] Y. Y. Gao, B. J. Lester, Y. Zhang, C. Wang, S. Rosenblum, L. Frunzio, L. Jiang, S. M. Girvin, and R. J. Schoelkopf, Programmable interference between two microwave quantum memories, arXiv:1802.08510 [quant-ph] (2018).

[10] F. R. Lescanne, L. Verney, Q. Ficheux, M. H. Devoret, B. Huard, M. Mirrahimi, and Z. Leghtas, arXiv:1805.05198 (2018).

[11] Jens Koch, Terri M. Yu, Jay Gambetta, A. A. Houck, D. I. Schuster, J. Majer, Alexandre Blais, M. H. Devoret, S. M. Girvin, and R. J. Schoelkopf, Charge-insensitive qubit design derived from the Cooper pair box, Phys. Rev. A **76**, 042319 (2007).

[12] Hanhee Paik, D. I. Schuster, Lev S. Bishop, G. Kirchmair, G. Catelani, A. P. Sears, B. R. Johnson, M. J. Reagor, L. Frunzio, L. I. Glazman, S. M. Girvin, M. H. Devoret, and R. J. Schoelkopf, Observation of High Coherence in Josephson Junction Qubits Measured in a Three-Dimensional Circuit QED Architecture, Phys. Rev. Lett. **107**, 11 (2011).

[13] M. D. Reed, L. DiCarlo, B. R. Johnson, L. Sun, D. I. Schuster, L. Frunzio, and R. J. Schoelkopf, High-Fidelity Readout in Circuit Quantum Electrodynamics Using the Jaynes-Cummings Nonlinearity, Phys. Rev. Lett. **105**, 173601 (2010).

[14] Erwan Faou, *Geometric Numerical Integration and Schrödinger Equations* (European Mathematical Society Publishing House, Zürich, 2012).

[15] Daniel Sank, Zijun Chen, Mostafa Khezri, J. Kelly, R. Barends, B. Campbell, Y. Chen, B. Chiaro, A. Dunsworth, A. Fowler, E. Jeffrey, E. Lucero *et al.*, Measurement-Induced State Transitions in a Superconducting Qubit: Beyond the Rotating Wave Approximation, Phys. Rev. Lett. **117**, 190503 (2016).

[16] I. Pietikäinen, S. Danilin, K. S. Kumar, A. Vepsäläinen, D. S. Golubev, J. Tuorila, and G. S. Paraoanu, Observation

of the Bloch-Siegert shift in a driven quantum-to-classical transition, Phys. Rev. B **96**, 020501 (2017).

[17] Milena Grifoni and Peter Hänggi, Driven quantum tunneling, Phys. Rep. **304**, 229 (1998).

[18] M. H. Devoret, Quantum Fluctuations in Electrical Circuits, in *Fluctuations Quantiques/Quantum Fluctuations*, edited by S. Reynaud, E. Giacobino, and J. Zinn-Justin (Amsterdam, 1997), p. 351.

[19] Crispin Gardiner and Peter Zoller, *Quantum Noise: A Handbook of Markovian and Non-Markovian Quantum Stochastic Methods with Applications to Quantum Optics (Springer Series in Synergetics)* (Springer, Berlin, 2004).

[20] The simulations were run on a workstation with Python 3.5.2 and a modified version of Qutip 4.2.0 [39].

[21] D. I. Schuster, A. Wallraff, A. Blais, L. Frunzio, R.-S. Huang, J. Majer, S. M. Girvin, and R. J. Schoelkopf, AC Stark Shift and Dephasing of a Superconducting Qubit Strongly Coupled to a Cavity Field, Phys. Rev. Lett. **94**, 123602 (2005).

[22] F. R. Ong, M. Boissonneault, F. Mallet, A. Palacios-Laloy, A. Dewes, A. C. Doherty, A. Blais, P. Bertet, D. Vion, and D. Esteve, Circuit QED with a Nonlinear Resonator: ac-Stark Shift and Dephasing, Phys. Rev. Lett. **106**, 167002 (2011).

[23] Matti Silveri, Jani Tuorila, Mika Kemppainen, and Erkki Thuneberg, Probe spectroscopy of quasienergy states, Phys. Rev. B **87**, 11 (2013).

[24] I. Pietikäinen, S. Danilin, K. S. Kumar, J. Tuorila, and G. S. Paraoanu, Observation of the Bloch-Siegert shift in a driven quantum-to-classical transition, J. Low Temp. Phys. **191**, 354 (2018).

[25] Jay Gambetta, Alexandre Blais, D. I. Schuster, A. Wallraff, L. Frunzio, J. Majer, M. H. Devoret, S. M. Girvin, and R. J. Schoelkopf, Qubit-photon interactions in a cavity: Measurement-induced dephasing and number splitting, Phys. Rev. A **74**, 042318 (2006).

[26] Brian Vlastakis, Gerhard Kirchmair, Zaki Leghtas, Simon E. Nigg, Luigi Frunzio, S. M. Girvin, Mazyar Mirrahimi, M. H. Devoret, and R. J. Schoelkopf, Deterministically encoding quantum information using 100-photon Schrödinger cat states, Science **342**, 607 (2013).

[27] Lev S. Bishop, Eran Ginossar, and S. M. Girvin, Response of the Strongly Driven Jaynes-Cummings Oscillator, Phys. Rev. Lett. **105**, 100505 (2010).

[28] Maxime Boissonneault, J. M. Gambetta, and Alexandre Blais, Improved Superconducting Qubit Readout by Qubit-Induced Nonlinearities, Phys. Rev. Lett. **105**, 100504 (2010).

[29] Th. K. Mavrogordatos, G. Tancredi, M. Elliott, M. J. Peterer, A. Patterson, J. Rahamim, P. J. Leek, E. Ginossar, M. H. Szymań, Simultaneous Bistability of a Qubit and Resonator in Circuit Quantum Electrodynamics, Phys. Rev. Lett. **118**, 040402 (2017).

[30] Matthew Elliott and Eran Ginossar, Applications of the Fokker-Planck equation in circuit quantum electrodynamics, Phys. Rev. A **94**, 043840 (2016).

[31] J. Koch, V. E. Manucharyan, M. H. Devoret, and L. Glazman, Charging Effects in the Inductively Shunted Josephson Junction, Phys. Rev. Lett. **103**, 217004 (2009).

[32] J. Braumülcer, M. Sandberg, M. R. Vissers, A. Schneider, S. Schlör, L. Grünhaupt, H. Rotzinger, M. Marthaler, A. Lukashenko, A. Dieter, A. V. Ustinov, M. Weides, and D. P. Pappas, Concentric transmon qubit featuring fast tunability and an anisotropic magnetic dipole moment, Appl. Phys. Lett. **108**, 032601 (2016).

[33] S. Richer, N. Maleeva, S. T. Skacel, I. M. Pop, and D. DiVincenzo, Inductively shunted transmon qubit with tunable transverse and longitudinal coupling, Phys. Rev. B **96**, 174520 (2017).

[34] J. E. Mooij, T. P. Orlando, L. Levitov, Lin Tian, Casper H. van der Wal, Seth Lloyd, Josephson persistent-current qubit, Science **285**, 1036 (1999).

[35] Vladimir E. Manucharyan, Jens Koch, Leonid I. Glazman, and Michel H. Devoret, Fluxonium: Single Cooper-pair circuit free of charge offsets, Science **326**, 113 (2009).

[36] N. E. Frattini, U. Vool, S. Shankar, A. Narla, K. M. Sliwa, and M. H. Devoret, 3-wave mixing Josephson dipole element, Appl. Phys. Lett. **110**, 222603 (2017).

[37] Mazyar Mirrahimi and Pierre Rouchon, Dynamics and control of open quantum systems, https://who.rocq.inria.fr/Mazyar.Mirrahimi/QuantSys2015.pdf, accessed: 2018-03-06.

[38] S. O. Mundhada, S. Shankar, A. Narla, E. Zalys-Geller, S. M. Girvin, and M. H. Devoret, Dependence of transmon qubit relaxation rate on readout drive power, in *APS Meeting Abstracts* (American Physical Society, Baltimore, 2016), p. V48.005.

[39] Robert Johansson, Paul Nation, Anubhav Vardhan, Alexander Pitchford, Chris Granade, Arne Løhre Grimsmo, Markus Baden, Piotr Migdal, Kevin Fischer, Denis Vasilyev *et al.*, qutip/qutip: QuTiP 4.2.0 (2017).

[40] J. R. Johansson, P. D. Nation, and F. Nori, Qutip 2: An open-source Python framework for the dynamics of open quantum systems, Comput. Phys. Commun. **184**, 1234 (2013).

[41] J. D. Hunter, MATPLOTLIB: A 2D graphics environment, Comput. Sci. Eng. **9**, 90 (2007).